



Solvent-free selective hydrogenation of nitroaromatics to azoxy compounds over Co single atoms decorated on Nb₂O₅ nanomeshes

Received: 5 August 2023

Accepted: 1 April 2024

Published online: 12 April 2024

Check for updates

Zhijun Li¹✉, Xiaowen Lu^{1,6}, Cong Guo^{2,6}, Siqi Ji¹, Hongxue Liu¹, Chunmin Guo¹, Xue Lu¹, Chao Wang³, Wensheng Yan³, Bingyu Liu⁴, Wei Wu⁴, J. Hugh Horton^{1,5}, Shixuan Xin¹ & Yu Wang²✉

The solvent-free selective hydrogenation of nitroaromatics to azoxy compounds is highly important, yet challenging. Herein, we report an efficient strategy to construct individually dispersed Co atoms decorated on niobium pentaoxide nanomeshes with unique geometric and electronic properties. The use of this supported Co single atom catalysts in the selective hydrogenation of nitrobenzene to azoxybenzene results in high catalytic activity and selectivity, with 99% selectivity and 99% conversion within 0.5 h. Remarkably, it delivers an exceptionally high turnover frequency of 40377 h⁻¹, which is amongst similar state-of-the-art catalysts. In addition, it demonstrates remarkable recyclability, reaction scalability, and wide substrate scope. Density functional theory calculations reveal that the catalytic activity and selectivity are significantly promoted by the unique electronic properties and strong electronic metal-support interaction in Co₁/Nb₂O₅. The absence of precious metals, toxic solvents, and reagents makes this catalyst more appealing for synthesizing azoxy compounds from nitroaromatics. Our findings suggest the great potential of this strategy to access single atom catalysts with boosted activity and selectivity, thus offering blueprints for the design of nanomaterials for organocatalysis.

Selective hydrogenation of nitrobenzene is an important reaction used to generate valued chemicals including nitrosobenzene, phenylhydroxylamine, aniline, azobenzene, and azoxybenzene^{1,2}. Of these, azoxybenzene and its derivatives are a class of compounds that have many potential applications in dyes, pharmaceuticals,

polymerization inhibitors, and food additives³. However, the complex reduction steps and low selectivity to azoxybenzene make this reaction challenging^{4,5}. Therefore, the design of a highly selective catalyst with moderate catalytic reduction abilities towards azoxybenzene is appealing. Among most of the metals, palladium,

¹National Key Laboratory of Continental Shale Oil, College of Chemistry and Chemical Engineering, Northeast Petroleum University, Daqing, PR China.

²Jiangsu Collaborative Innovation Centre of Biomedical Functional Materials, School of Chemistry and Materials Science, Nanjing Normal University, Nanjing, PR China. ³National Synchrotron Radiation Laboratory, University of Science and Technology of China, Hefei, PR China. ⁴National Center for International Research on Catalytic Technology, School of Chemistry and Material Sciences, Heilongjiang University, Harbin, PR China. ⁵Department of Chemistry, Queen's University, Kingston, Canada. ⁶These authors contributed equally: Xiaowen Lu, Cong Guo. ✉e-mail: zhijun.li@queensu.ca;

yu.wang@njnu.edu.cn

iridium, and rhodium are typically used as active catalysts for selective hydrogenation reactions^{6–8}. However, the high cost has greatly restricted the wide use of these precious metal-based catalysts. Moreover, strong bases or expensive organic reducing agents are typically employed in the reaction⁹. Therefore, the development of sustainable, environmentally benign, and low-cost catalysts for the selective hydrogenation of nitroaromatics to azoxy compounds is highly desirable.

Selectivity and activity in catalysis are important for efficiently producing commodity chemicals, fine chemicals, and pharmaceuticals¹⁰. Both factors are determined by the adsorption characteristics and activation ability of catalytically active sites toward reactants, intermediates, and products. These in turn are influenced by the geometric and electronic properties of these sites^{11,12}. In homogeneous catalysis, the properties of these sites may be effectively tuned by steric and electronic structures; however, fine-tuning the selectivity in heterogeneous catalysis is challenging^{10,13,14}. In addition to the catalytic activity-selectivity relationship, solvent waste removal also poses a formidable challenge for green chemical synthesis and energy consumption¹⁵. The use of solvent-free mechanical methods (grinding or milling) for reagents mixing and activation holds many advantages, such as shortened reaction periods, mild reaction conditions, and excellent selectivity to the target products^{16–18}. Therefore, there is a strong incentive to construct highly active and selective catalyst systems that do not require the use of solvent to efficiently hydrogenate nitroaromatics to the corresponding azoxy compounds using H₂^{19,20}.

Recent years have witnessed the fast development of single atom catalysts (SACs) with unique coordination environments, high atom utilization, and appealing catalytic efficacy in a number of chemical reactions^{14,21,22}. Notably, SACs possess almost 100% atomic dispersion and high activity for each active metal sites^{22,23}. In addition, they can elegantly bridge heterogeneous and homogeneous catalysis to endow exceptional activity, selectivity, and stability^{24,25}. The catalytic performance of SACs can be improved by adjusting the coordination environment and electronic properties of metal active sites, which are generally influenced by synthetic methods and support materials^{26–30}. Modulating the electron coupling between metals and supports can effectively regulate the electronic structure of metal sites for improved catalytic efficacy^{31,32}. Niobium pentoxide (Nb₂O₅) is an important catalyst support material due to its high stability, moderate acidity, and excellent C–O and C–C bond cleavage ability^{33,34}. Nb₂O₅-supported metal catalysts have found applications in a variety of catalytic reactions, including hydrodeoxygenation, C–O bond activation, C_{aromatic}–C bonds cleavage, and aldol condensation^{35–37}. However, the use of Nb₂O₅ as a support material for decoration of isolated non-precious metal atoms in organocatalysis has been rarely reported.

Herein, we report a facile and reliable strategy to synthesize atomically dispersed Co atoms anchored on niobium pentoxide (Co₁/Nb₂O₅) nanomeshes. Aberration-corrected high-angle annular dark-field scanning transmission electron microscopy (AC HAADF-STEM), X-ray absorption spectroscopy (XAFS), and X-ray photoelectron spectroscopy (XPS) confirm the Co atoms in Co₁/Nb₂O₅ are atomically dispersed and positively charged. This non-precious metal-based catalyst delivers exceptional catalytic efficacy on solvent-free selective hydrogenation of nitroaromatics to azoxy compounds under base-free and solvent-free conditions (Fig. 1). The as-prepared Co₁/Nb₂O₅ has the potential to bypass the limitations of previously reported catalysts and enable rapid and efficient access to a diverse range of azoxy compounds from functionalized nitroaromatics. Theoretical studies reveal that the unique electronic structure and strong electronic metal-support coupling effect between Co atoms with support atoms in close proximity are beneficial for the efficient activation of reactants.

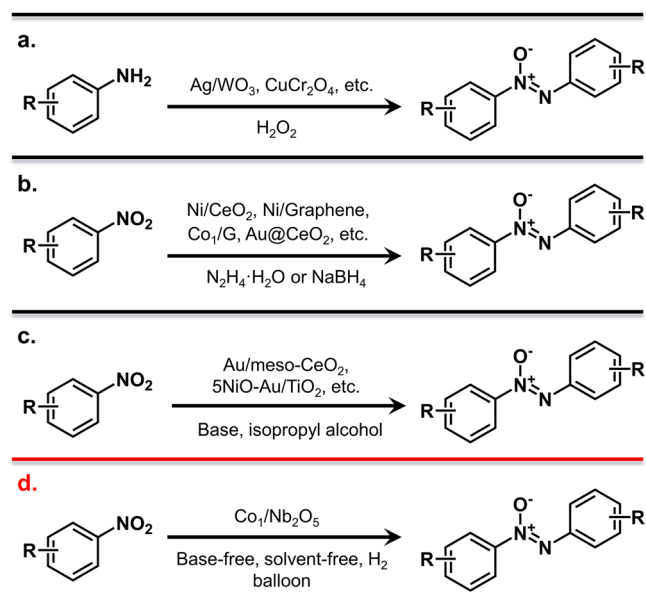


Fig. 1 | Representative examples for the synthesis of azoxy compounds.

a Oxidation of anilines into aromatic azoxy compounds. **b** Reduction of nitroarenes to aromatic azoxy compounds. **c** Hydrogenation of nitroarenes to aromatic azoxy compounds with noble metal catalyst in the presence of base. **d** This work: Direct hydrogenation of nitroarenes into aromatic azoxy compounds with non-noble metal catalysts under base-free and solvent-free conditions.

Results

Synthesis and characterization of atomically dispersed Co catalyst

An efficient two-step strategy (Fig. 2a) incorporating incipient wetness impregnation and microwave irradiation procedures was developed to create individually dispersed cobalt atoms over niobium pentoxide nanomeshes (Co₁/Nb₂O₅). Typically, Nb₂O₅ was prepared by reacting ammonium niobate oxalate hydrate, melamine, and ammonium chloride in ethanol, followed by a calcination step in air. Electron microscopy characterization demonstrates that the as-prepared Nb₂O₅ possesses a nanomesh structure (Supplementary Figs. 1 and 2). Subsequently, the as-prepared Nb₂O₅ was homogeneously mixed with cobalt acetate aqueous solution by an incipient wetness impregnation approach (Co²⁺@Nb₂O₅). After drying by an infrared lamp, the dried powder was microwave-treated at 800 W for 10 s to obtain Co₁/Nb₂O₅ with cobalt loading of 0.42 wt% and cobalt dispersion of 97% (Supplementary Table 1). This suggests that the vast majority of Co species were in the form of isolated Co atoms in Co₁/Nb₂O₅. Similar nanomesh morphologies between Co₁/Nb₂O₅ and Nb₂O₅ are observed by electron microscopy characterizations (Fig. 2b–d and Supplementary Fig. 3). An average height of ~6 nm is observed for Co₁/Nb₂O₅ as measured by atomic force microscope (AFM) imaging (Fig. 2d inset). Aberration-corrected HAADF-STEM imaging as shown in Fig. 2e displays lattice fringe spacings of 0.393 and 0.315 nm which correspond to the (001) and (180) facets of Nb₂O₅. The corresponding ring-like selected area electron diffraction (SAED) pattern is shown in Fig. 2e inset and agrees well with the previous reports^{38,39}. A magnified AC HAADF-STEM image reveals that the isolated Co atoms are distributed over the Nb₂O₅ surface (Fig. 2f). Note that the cobalt atom has a lower Z contrast relative to niobium atoms. Additionally, the enlarged area provides preliminary evidence for the presence of isolated Co atoms over the Nb₂O₅ surface (Fig. 2f inset). Energy-dispersive X-ray spectroscopy (EDS) analysis demonstrates the homogeneously distributed O, Co, and Nb over Nb₂O₅ surface (Fig. 2g). By contrast, a 5.12 wt% Co NPs-containing catalyst (Co NPs/Nb₂O₅, Co dispersion of 39%) was created with large metallic Co species (Supplementary Fig. 4 and Table 1).

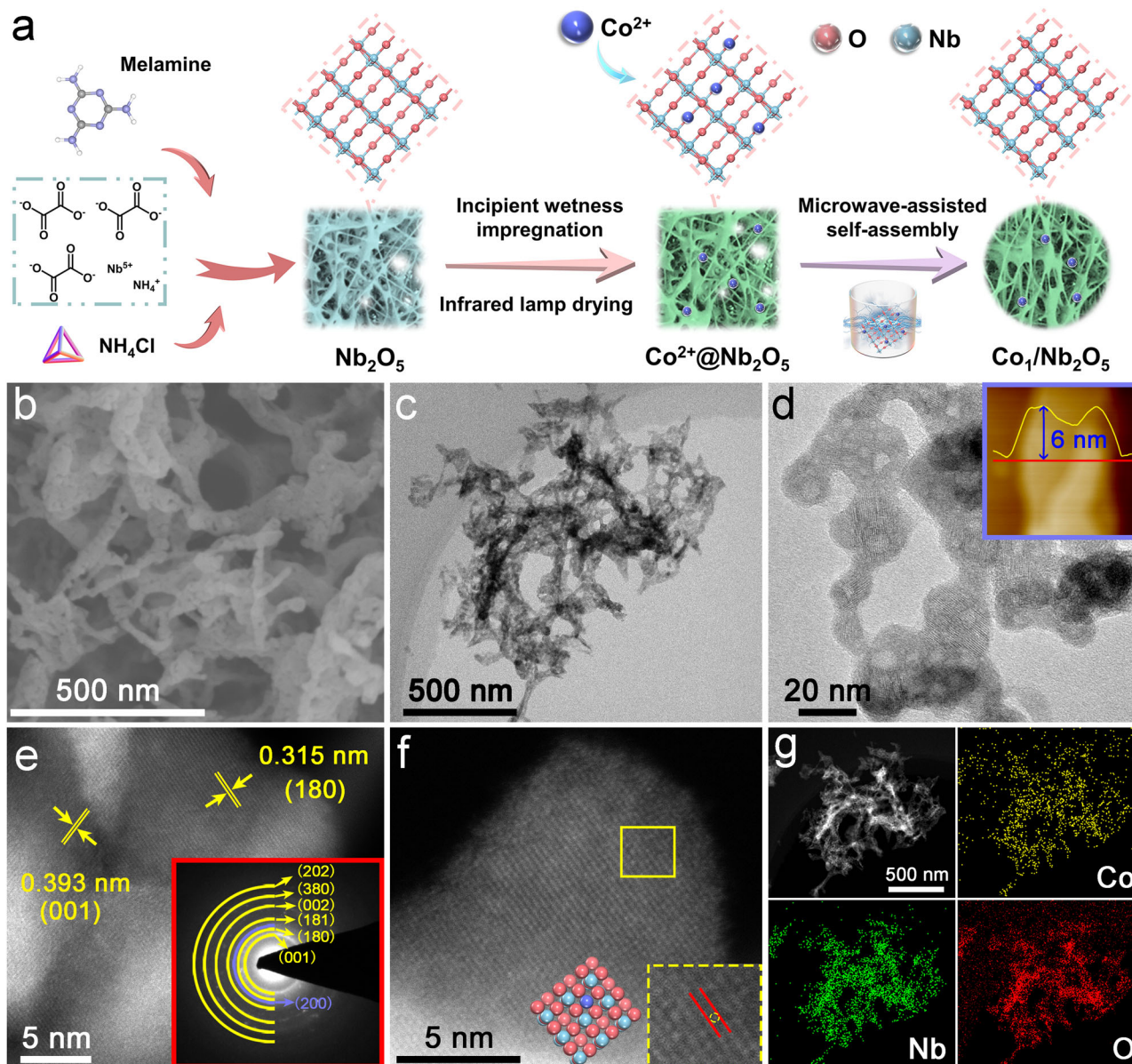


Fig. 2 | The synthesis strategy and characterizations of $\text{Co}_1/\text{Nb}_2\text{O}_5$. **a** Schematic illustration of the synthesis strategy. **b** SEM image. **c** TEM image. **d** HR-TEM image (the inset is an AFM image showing the height profile). **e** AC HAADF-STEM image

(the inset is SAED pattern). **f** AC HAADF-STEM image at high magnification. The red, blue, and purple atoms represent O, Nb, and Co, respectively. **g** EDS mapping images.

X-ray diffraction (XRD) patterns of samples are exhibited in Fig. 3a. Typical diffraction peaks of Nb_2O_5 (JCPDS No. 30-0873) agree well with SAED patterns as shown in Fig. 2e. Moreover, there are no evident metallic cobalt peaks found in $\text{Co}_1/\text{Nb}_2\text{O}_5$, suggesting that these Co species are highly dispersed on the Nb_2O_5 surface, even for Co NPs/ Nb_2O_5 . Raman spectra are shown in Fig. 3b. The overlapped Raman signals are categorized into three band groups^{40,41}: a high-wavenumber (ν_{Hi} , 485 cm^{-1} - 808 cm^{-1}), a mid-wavenumber (ν_{Mid} , 175 - 370 cm^{-1}), and a low-wavenumber band group (ν_{Lo} , 93 - 172 cm^{-1}). The peaks in the 100 - 400 cm^{-1} region are associated with typical bending modes of Nb-O-Nb linkages⁴¹. After Co deposition, the intensities of peaks at 120 cm^{-1} in $\text{Co}_1/\text{Nb}_2\text{O}_5$ and Co NPs/ Nb_2O_5 are enhanced, while the peaks at 230 cm^{-1} are weakened. This suggests the formation of Co-O-Nb linkages and disordering of the bending modes in Nb_2O_5 ⁴¹. In addition, the initially high-intensity peak at 690 cm^{-1} is reduced significantly due to the Co deposition partially distorting the Nb_2O_5 structure^{41,42}. X-ray photoelectron spectroscopy (XPS) was conducted to understand the electronic properties of samples (Fig. 3c

and Supplementary Fig. 5). Compared with the Co NPs/ Nb_2O_5 sample (Fig. 3c), the Co $2p_{3/2}$ peak of $\text{Co}_1/\text{Nb}_2\text{O}_5$ is located at 781.1 eV, agreeing well with assignment as a positively charged Co species^{43,44}. The O 1s and Nb $3d$ spectra of $\text{Co}_1/\text{Nb}_2\text{O}_5$ and Co NPs/ Nb_2O_5 are shown in Supplementary Fig. 5c. We observe surface oxygen vacancies in both samples, indicating the presence of electronic coupling interaction between the introduced Co species and the Nb_2O_5 support⁴⁵. The Nb $3d$ spectra of both samples can be fitted to two peaks for Nb $3d_{5/2}$ and Nb $3d_{3/2}$, respectively. The position of the Nb $3d_{5/2}$ peak of $\text{Co}_1/\text{Nb}_2\text{O}_5$ is centered at 207.1 eV, which is slightly lower than that of Co NPs/ Nb_2O_5 (207.3 eV), suggesting a relatively larger concentration of Nb⁴⁺ species and oxygen vacancies over the former⁴⁶. Nonetheless, the chemical shift suggests that only a small portion of the niobium present in either sample is in the form of Nb⁴⁺ species. In situ CO-diffuse reflectance infrared Fourier transform spectroscopy (CO-DRIFTS) was performed to investigate atomic structures of Co species in $\text{Co}_1/\text{Nb}_2\text{O}_5$ and Co NPs/ Nb_2O_5 (Fig. 3d). The broad bands around 2171 cm^{-1} and 2115 cm^{-1} are ascribed to residual gas-phase CO molecules^{47,48}. For $\text{Co}_1/\text{Nb}_2\text{O}_5$, a

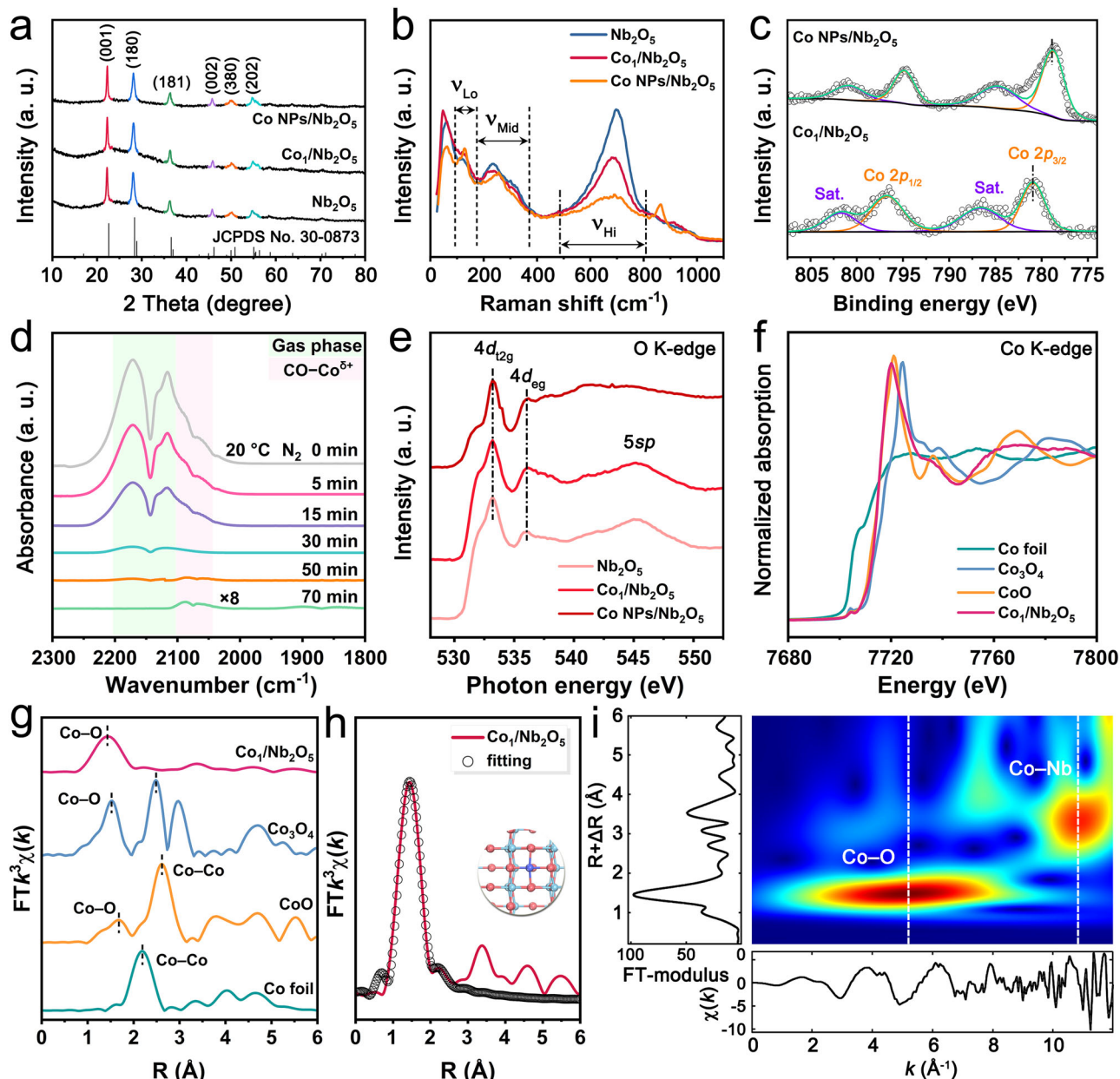


Fig. 3 | Structural characterizations of as-prepared $\text{Co}_1/\text{Nb}_2\text{O}_5$. **a** XRD patterns. **b** Raman spectra. **c** XPS $\text{Co } 2p$ spectra. **d** In situ CO-DRIFTS of $\text{Co}_1/\text{Nb}_2\text{O}_5$. **e** O K-edge spectra. **f** XANES spectra at Co K-edge. **g** Fourier transformed k^3 -weighted Co

K-edge of EXAFS spectra. **h** EXAFS fitting in R space (inset is the model of $\text{Co}_1\text{-O}_4$). **i** 3D contour WT-EXAFS plot.

pair of CO adsorption peaks were observed at 2089 cm^{-1} and 2067 cm^{-1} , respectively, which could be assigned to linearly adsorbed CO on positively charged Co species^{49,50}. The absence of other peaks excludes the presence of Co multiatomic species in $\text{Co}_1/\text{Nb}_2\text{O}_5$. In the case of Co NPs/ Nb_2O_5 , two peaks appeared at 2015 cm^{-1} and 1984 cm^{-1} , respectively, which are associated with the CO adsorbing on metallic Co in linear and bridge form (Supplementary Fig. 6)⁵¹. Electron paramagnetic resonance (EPR) spectra (Supplementary Fig. 7) demonstrate a sharp signal at a g value of 2.003 for $\text{Co}_1/\text{Nb}_2\text{O}_5$, which is associated with the coordinatively unsaturated Co species in the catalyst⁴⁵. H_2 -temperature-programmed reduction (H_2 -TPR) results are shown in Supplementary Fig. 8. Two peaks at $508\text{ }^\circ\text{C}$ and $588\text{ }^\circ\text{C}$ are observed for Nb_2O_5 , corresponding to surface Nb–O–Nb and interior Nb–O–Nb sites⁴⁶. After introducing Co species, only two peaks at $341\text{ }^\circ\text{C}$ and $484\text{ }^\circ\text{C}$ are observed, which are associated with the reduction of Co–O–Nb and interior Nb–O–Nb species, respectively. This suggests

Nb_2O_5 can serve as a heterogeneous support for anchoring the isolated Co atoms and restricting them from agglomeration.

To understand the chemical state of Co species in the catalysts, Co $L_{2,3}$ -edge near-edge X-ray absorption fine structure (NEXAFS) results were collected with synchrotron-based soft X-ray radiation. As shown in Supplementary Fig. 9, the peak of the Co L-edge spectrum in $\text{Co}_1/\text{Nb}_2\text{O}_5$ displays a positive shift of 0.9 eV relative to that of Co NPs/ Nb_2O_5 , indicating a higher valence state of Co in $\text{Co}_1/\text{Nb}_2\text{O}_5$ ^{52,53}. This is in good agreement with the XPS results as discussed in Fig. 3c. O K-edge NEXAFS spectra (Fig. 3e) exhibit a lowered $4d_{t_{2g}}$ peak intensity for O–Nb coupling after deposition of Co species in Nb_2O_5 . These results, in conjunction with the XPS O $1s$ spectra, demonstrate that the $\text{Co}_1/\text{Nb}_2\text{O}_5$ and Co NPs/ Nb_2O_5 interfaces facilitate the formation of oxygen vacancies in these catalysts⁵⁴. Synchrotron radiation-based ultraviolet photoemission spectroscopy (UPS) was performed to study the electronic state of $\text{Co}_1/\text{Nb}_2\text{O}_5$ and Co NPs/ Nb_2O_5 . As displayed in

Supplementary Fig. 10, the values of valence band maxima for $\text{Co}_1/\text{Nb}_2\text{O}_5$ and $\text{Co NPs}/\text{Nb}_2\text{O}_5$ are determined to be 2.27 eV and 2.56 eV, respectively. This indicates a change in the electron arrangement of Co 3d orbitals, which is associated with the metal-support interaction and the coordination environment. Because the valence electrons near the Fermi level contribute greatly to the d states, the change in the valence band signifies the movement of the d band center. Fourier-transform infrared (FT-IR) spectra of samples are shown in Supplementary Fig. 11 and signals typical of Nb–O–Nb and Nb=O are observed. N_2 adsorption/desorption isotherms (Supplementary Fig. 12 and Table 1) show the specific surface area of Nb_2O_5 , $\text{Co}_1/\text{Nb}_2\text{O}_5$, and $\text{Co NPs}/\text{Nb}_2\text{O}_5$ are determined to be 49.8, 56.7, and 80.0 m^2/g , respectively. TGA/DSC results show similar results for $\text{Co}_1/\text{Nb}_2\text{O}_5$ and $\text{Co NPs}/\text{Nb}_2\text{O}_5$ (Supplementary Fig. 13). This implies that the incorporation of Co species into Nb_2O_5 did not significantly affect the material properties.

The atomic dispersion and coordination information of Co species in $\text{Co}_1/\text{Nb}_2\text{O}_5$ were examined by synchrotron-radiation X-ray absorption fine structure spectroscopy (XAFS). As disclosed in Fig. 3f, the pre-edge of Co K-edge in $\text{Co}_1/\text{Nb}_2\text{O}_5$ is located between those of CoO and Co_3O_4 , and closer to that of CoO. This indicates the valence state of Co species is between Co^{2+} and Co^{3+} , though closer to Co^{2+} . The positively charged Co species result from the strong charge transfer between atomically dispersed Co species and the Nb_2O_5 support⁵⁵. In the k-space of the extended X-ray absorption fine structure spectra (EXAFS), $\text{Co}_1/\text{Nb}_2\text{O}_5$ displays a different pattern compared with Co foil (Supplementary Fig. 14), implying they possess different coordination structures. Figure 3g shows the Fourier-transformed k^3 -weighted EXAFS spectra of Co in $\text{Co}_1/\text{Nb}_2\text{O}_5$ together with other reference samples. The Co foil reference exhibits a dominant peak at 2.19 Å that is associated with Co–Co scattering in the first coordination sphere. CoO displays two peaks at 1.67 Å and 2.62 Å that can be indexed to Co–O and Co–Co scattering, respectively. Co_3O_4 exhibits two peaks at 1.52 Å and 2.49 Å, also corresponding to Co–O and Co–Co scattering, respectively. As for $\text{Co}_1/\text{Nb}_2\text{O}_5$, there is only one prominent peak centered at 1.43 Å and this is assigned to Co–O scattering in the first shell. These results confirm the atomic distribution of Co species in $\text{Co}_1/\text{Nb}_2\text{O}_5$. The EXAFS fitting results (Fig. 3h, Supplementary Fig. 15 and Table 2) reveal that the Co atom is encircled by oxygen atoms with an average coordination number of 4.6. Wavelet transform (WT) results (Fig. 3i and Supplementary Fig. 16) confirm the presence of Co–O bond in $\text{Co}_1/\text{Nb}_2\text{O}_5$, in line with the Co K-edge FT-EXAFS analysis. Together, these findings demonstrate an atomic dispersion of Co species over Nb_2O_5 support.

Evaluation of catalytic performance

The catalytic performance of $\text{Co}_1/\text{Nb}_2\text{O}_5$ in the selective hydrogenation of nitrobenzene to azoxybenzene was initially evaluated under 1 atm of H_2 at 20 °C with addition of solvent (Supplementary Table 3). A series of solvents were screened and the use of tetrahydrofuran/ H_2O (4:1, v:v) mixed solvents secured the optimum reaction conditions (Supplementary Table 4). We observe low catalytic activity in the case of Nb_2O_5 , implying the Co species are essential for the catalytic performance (Supplementary Table 5). With $\text{Co}_1/\text{Nb}_2\text{O}_5$, the reaction proceeds smoothly to give the desired azoxybenzene with high conversion (99%) and selectivity (99%) within 1.5 h (Supplementary Fig. 17 and Table 5). No side product of aniline is detected for this reaction. Various Co salts, including $\text{Co}(\text{NO}_3)_2$, $\text{Co}(\text{Ac})_2$, CoCl_2 , and CoPc , are unable to efficiently catalyze this transformation, resulting in low catalytic activity (Supplementary Table 5). Accordingly, an extremely high turnover frequency (TOF) value of 11524 h^{-1} is noted for $\text{Co}_1/\text{Nb}_2\text{O}_5$ compared with the control samples. For $\text{Co NPs}/\text{Nb}_2\text{O}_5$ (Supplementary Fig. 18 and Table 5), aniline is identified as the main product with a high selectivity of 99%, together with trace amounts of azoxybenzene and azobenzene.

Next, we sought to investigate the catalytic efficacy of $\text{Co}_1/\text{Nb}_2\text{O}_5$ in catalyzing this reaction under solvent-free conditions. We observed an exceptionally high catalytic activity of $\text{Co}_1/\text{Nb}_2\text{O}_5$, with maximized atomic utilization. The reaction yielded azoxybenzene with excellent conversion (99%) and exclusive selectivity (99%) within merely 0.5 h (Fig. 4a and Supplementary Fig. 19). Additionally, the 99% selectivity remains unchanged following a further 9.5 h reaction, emphasizing excellent catalyst performance. This implies that the undesired side reaction was effectively constrained in the absence of Co–Co bonds. In the case of $\text{Co NPs}/\text{Nb}_2\text{O}_5$, aniline is the main product (Fig. 4b). This might result from the aggregated Co species over Nb_2O_5 with multiple Co–Co bonds. Catalysts consisting of Co single atoms anchored on other oxides using the same synthetic method with O-coordination structures were also prepared, being Co_1/MgO and $\text{Co}_1/\text{V}_2\text{O}_5$, respectively (Supplementary Figs. 20 and 21, and Table 2). A nitrogen-doped carbon support with Co single atoms ($\text{Co}_1/\text{N-C}$) was fabricated to represent different coordination environments, for example, Co–N coordination (Supplementary Fig. 22 and Table 2). Remarkably, an exceptional TOF value of 40377 h^{-1} for $\text{Co}_1/\text{Nb}_2\text{O}_5$ was determined, significantly higher than other control samples (Fig. 4c). Poor catalytic activity and selectivity of Co_1/MgO , $\text{Co}_1/\text{V}_2\text{O}_5$, and $\text{Co}_1/\text{N-C}$ are observed (Supplementary Fig. 23). This might result from the unique coordination environments, electronic structures, and electronic metal-support interactions of catalytically active Co sites in $\text{Co}_1/\text{Nb}_2\text{O}_5$ that influence the reaction pathways and energy barriers. Under these mild conditions, $\text{Co}_1/\text{Nb}_2\text{O}_5$ also demonstrates superior catalytic performance compared with previously reported catalysts (Supplementary Table 6).

Kinetic studies were performed to gain more insights into the origin of the catalytic activity of $\text{Co}_1/\text{Nb}_2\text{O}_5$ based on initial conversion rates of nitrobenzene at different temperatures (Fig. 4d and Supplementary Fig. 24). Compared with $\text{Co NPs}/\text{Nb}_2\text{O}_5$, a lowered activation energy (E_a) of 39 kJ mol^{-1} was determined for $\text{Co}_1/\text{Nb}_2\text{O}_5$ which suggests an enhanced catalytic activity. This offers evidence that the functionalization of a moderate amount of atomically dispersed Co atoms over Nb_2O_5 can significantly boost the catalytic activity. After 10 cycles of repetitive use, this $\text{Co}_1/\text{Nb}_2\text{O}_5$ catalyst exhibits admirable stability without noticeable activity degradation (Fig. 4e and Supplementary Table 7). The crystalline structure and morphology of recycled $\text{Co}_1/\text{Nb}_2\text{O}_5$ catalyst do not show any evident differences (Supplementary Fig. 25). Importantly, the EXAFS results of spent $\text{Co}_1/\text{Nb}_2\text{O}_5$ catalyst (Supplementary Fig. 26 and Table 2) demonstrate that the dispersion and coordination environment of Co atoms are unchanged after 10 cycles. In addition, Co L-edge and O K-edge NEXAFS (Supplementary Fig. 27) reveal that no substantial electronic structural changes were observed. These results imply a strong metal-support interaction in the $\text{Co}_1/\text{Nb}_2\text{O}_5$ catalyst with high stability.

H_2 dissociation ability over catalysts plays a crucial role in the hydrogenation reactions^{56–58}. H_2 -temperature-programmed desorption (H_2 -TPD) measurements were initially performed and the results (Supplementary Fig. 28) show that $\text{Co NPs}/\text{Nb}_2\text{O}_5$ exhibits a higher intensity of desorption peaks over $\text{Co}_1/\text{Nb}_2\text{O}_5$ and Nb_2O_5 , implying the existence of a higher amount of active sites and greater H_2 adsorption capacity (Supplementary Table 1). The desorption temperature of $\text{Co}_1/\text{Nb}_2\text{O}_5$ is slightly smaller than that of $\text{Co NPs}/\text{Nb}_2\text{O}_5$, but higher than that of Nb_2O_5 . Based on Kyriakou's work⁵⁹, the H_2 dissociation barrier will be lower on the active sites once the corresponding binding energy of dissociated H atoms is higher. Therefore, the higher H_2 desorption temperature of $\text{Co NPs}/\text{Nb}_2\text{O}_5$ suggests that it favors the activation and dissociation of H_2 more efficiently than $\text{Co}_1/\text{Nb}_2\text{O}_5$ and Nb_2O_5 . The H_2 dissociation activity of the samples was further evaluated using an H_2 - D_2 exchange experiment (Supplementary Fig. 29). The HD formation rate follows the order $\text{Co NPs}/\text{Nb}_2\text{O}_5 > \text{Co}_1/\text{Nb}_2\text{O}_5 > \text{Nb}_2\text{O}_5$. $\text{Co NPs}/\text{Nb}_2\text{O}_5$ achieved a higher HD

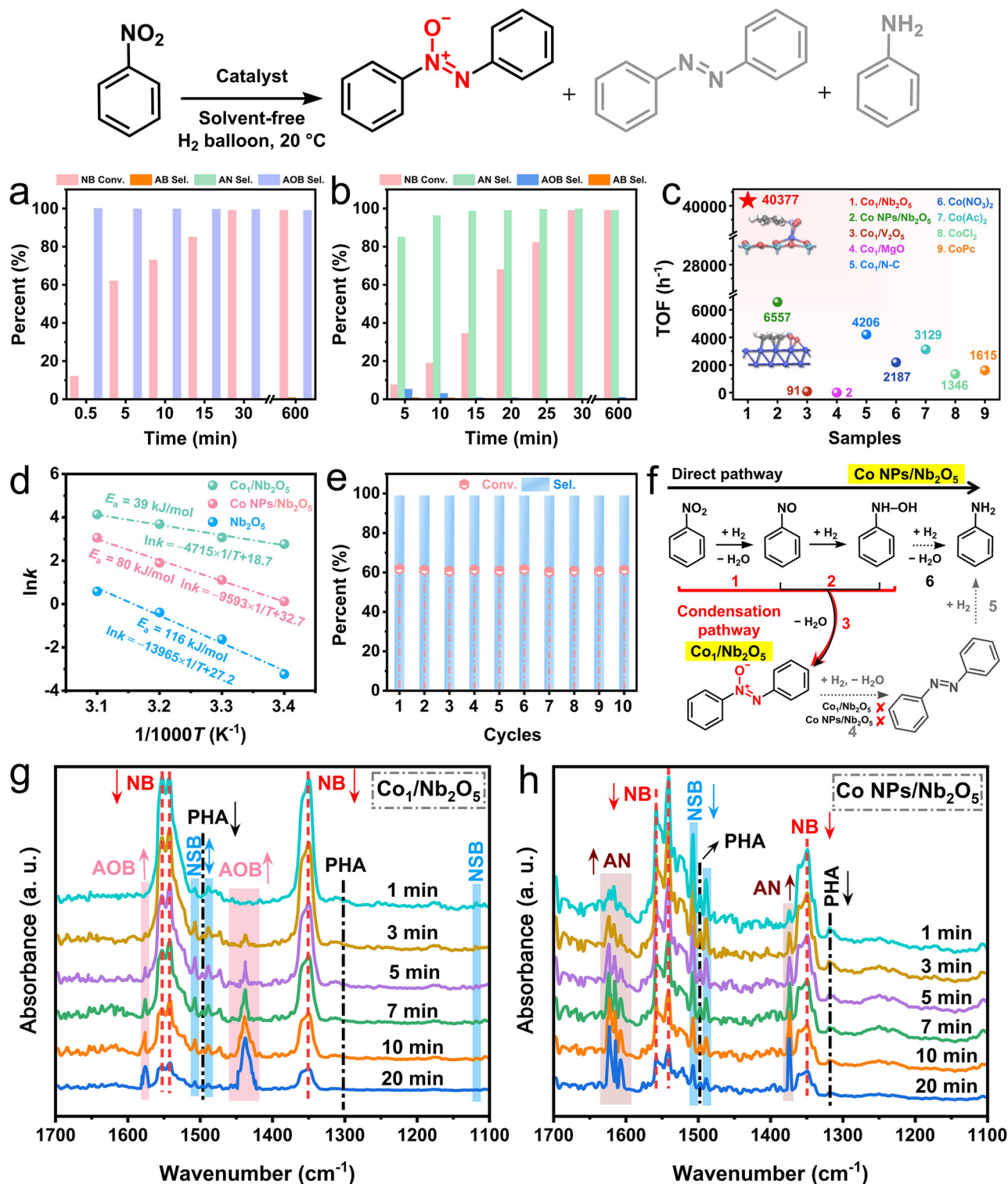


Fig. 4 | Catalytic performance of $\text{Co}_1/\text{Nb}_2\text{O}_5$ in the solvent-free selective hydrogenation of nitrobenzene to azoxybenzene. Conversion and selectivity of (a) $\text{Co}_1/\text{Nb}_2\text{O}_5$ and (b) $\text{Co NPs}/\text{Nb}_2\text{O}_5$. c The corresponding TOF values of different samples. d Arrhenius plots and E_a values. e Recycling results (Reaction time: 5 min).

f The proposed reaction routes. In situ DRIFTS spectra were recorded during the hydrogenation of nitrobenzene over (g) $\text{Co}_1/\text{Nb}_2\text{O}_5$ and (h) $\text{Co NPs}/\text{Nb}_2\text{O}_5$. (NB nitrobenzene; NSB nitrosobenzene; PHA phenylhydroxylamine; AB azobenzenze; AOB azoxybenzene; AN aniline).

formation rate than those of $\text{Co}_1/\text{Nb}_2\text{O}_5$ and Nb_2O_5 , suggesting that the addition of Co species could considerably enhance the H_2 dissociation activity and subsequently promote the hydrogenation reactions. Although $\text{Co NPs}/\text{Nb}_2\text{O}_5$ exhibits excellent nitrobenzene conversion, it exhibits extremely poor azoxybenzene selectivity. This implies that the difference in H_2 dissociation activity might not be the only reason

affecting the overall catalytic performance of the catalyst. More discussion on the origin of the selectivity difference can be found in the kinetics simulations of key hydrogenation steps in the Mechanism investigation section.

Based on these experimental findings, we assume that the $\text{Co}_1/\text{Nb}_2\text{O}_5$ follows the steps from 1-2-3, while the $\text{Co NPs}/\text{Nb}_2\text{O}_5$ take the

steps from 1-2-6 under the reaction conditions (Fig. 4f). To confirm this point, the selective hydrogenation of nitrobenzene was examined on $\text{Co}_1/\text{Nb}_2\text{O}_5$ and $\text{Co NPs}/\text{Nb}_2\text{O}_5$ by in situ DRIFTS. In the case of $\text{Co}_1/\text{Nb}_2\text{O}_5$ (Fig. 4g), the spectra show a slow consumption of nitrobenzene (IR bands at 1552, 1543, and 1349 cm^{-1})⁶⁰ and the appearance of azoxybenzene with rapidly increased IR bands^{9,61,62} at 1576 and 1437 cm^{-1} . The intermediate species of phenylhydroxylamine (1496 and 1302 cm^{-1})⁹ and nitrosobenzene (1507 and 1119 cm^{-1})^{9,61} were also observed. For $\text{Co NPs}/\text{Nb}_2\text{O}_5$ (Fig. 4h), the IR bands of nitrobenzene decrease gradually, while the bands of aniline (1623 , 1614 , 1606 , and 1375 cm^{-1})^{9,61} increase, indicating H_2 introduction favors the formation of aniline. In addition, we also observed the key reaction intermediate of nitrosobenzene and phenylhydroxylamine. These IR results are in excellent agreement with the experimental results. To validate the utility of the $\text{Co}_1/\text{Nb}_2\text{O}_5$ catalyst in large-scale organocatalysis, we scaled up the reaction (50-fold) to the gram scale and established optimized conditions (Supplementary Fig. 30). The results show the catalytic performance of $\text{Co}_1/\text{Nb}_2\text{O}_5$ was nearly identical to the lab-scale to give azoxybenzene, underscoring the potential of reaction scale tolerance.

With the optimized reaction conditions established, the substrate scope of solvent-free selective hydrogenation of nitroaromatics to azoxy compounds was explored. As shown in Fig. 5 and Supplementary Figs. 31–46, a variety of nitroaromatics were tested and all of these substrates are well tolerated and converted efficiently to the corresponding azoxy compounds in high conversion (up to 99%) and selectivity (up to 99%). The nitroaromatics bearing either electron-withdrawing substituents (halogen group, and nitro group) or electron-donating substituents (hydroxyl group, methoxyl group, methyl group, and amino group), situated at the *para*-position of the aromatic ring, did not have a noticeable impact on the reaction output. Note that methyl and methoxy groups at either *ortho*- or *meta*-positions (2r, 2o, 2l, 2j) underwent smooth conversion to afford the desired products with slightly lower efficacy compared to the more sterically accessible ones at *para*-position (2a, 2b). This might be due to the steric hindrance effect of the substituent groups that unfavor the coupling reactions. In addition to symmetrical azoxy compounds, we also tried to explore the potential feasibility of synthesizing products with unsymmetrical compounds (Supplementary Fig. 47). To our delight, this $\text{Co}_1/\text{Nb}_2\text{O}_5$ catalyst shows good reactivity and affords the desired unsymmetrical compounds in moderate yields in most cases. Together, the results demonstrate the developed $\text{Co}_1/\text{Nb}_2\text{O}_5$ catalyst can efficiently catalyze solvent-free selective hydrogenation of nitroaromatics to yield azoxy compounds.

Mechanism investigation

To explore the origin of the high catalytic performance of $\text{Co}_1/\text{Nb}_2\text{O}_5$ catalyst, density functional theory (DFT) calculations were performed. The optimized geometric structures of Nb_2O_5 , $\text{Co}_1/\text{Nb}_2\text{O}_5$, and $\text{Co NPs}/\text{Nb}_2\text{O}_5$ are shown in Supplementary Figs. 48–50. Based on AC STEM and XAFS characterizations, we embedded a Co atom on the $\text{Nb}_2\text{O}_5(001)$ surface to describe $\text{Co}_1/\text{Nb}_2\text{O}_5$ and employed Co(III) to represent $\text{Co NPs}/\text{Nb}_2\text{O}_5$ for the calculation. Bader charge and charge density difference analysis of $\text{Co}_1/\text{Nb}_2\text{O}_5$ indicate that the Co atom loses $0.83 e$ to the neighboring O atoms in $\text{Co}_1/\text{Nb}_2\text{O}_5$ (Fig. 6a and Supplementary Fig. 51). This suggests the presence of electronic metal-support interactions and the positively charged Co atoms. In addition, there is orbital mixing between O and Co atoms based on the projected density of states (PDOS) in $\text{Co}_1/\text{Nb}_2\text{O}_5$ relative to that of Nb_2O_5 , as shown in Fig. 6b and Supplementary Fig. 52. The *d* band centers of Co in $\text{Co}_1/\text{Nb}_2\text{O}_5$ and Co(III) were determined to be -2.95 eV and -2.09 eV , respectively (Fig. 6b, c). Figure 6d, e shows the reaction pathways and the corresponding calculated energy profiles over $\text{Co}_1/\text{Nb}_2\text{O}_5$ and Co(III) . The configurations of intermediates are displayed

in Supplementary Figs. 53 and 54. The nitrobenzene adsorption energies (E_{PhNO_2}) for $\text{Co}_1/\text{Nb}_2\text{O}_5$ and Co(III) were both calculated to be exothermic at -1.25 eV and -2.57 eV , respectively. The larger adsorption energy of Co(III) demonstrates it has a much stronger affinity to nitrobenzene, which is in good agreement with its *d* band center that is closer to the Fermi level than $\text{Co}_1/\text{Nb}_2\text{O}_5$. With $\text{Co}_1/\text{Nb}_2\text{O}_5$, the adsorbed $^*\text{PhNO}_2$ can be hydrogenated to afford a $^*\text{PhNO}_2\text{H}$ intermediate (-0.24 eV) and then form $^*\text{PhNO}$ (-1.61 eV). Subsequently, the $^*\text{PhNO}$ intermediate would be reduced to $^*\text{PhNOH}$ and then $^*\text{PhN}$ via two hydrogenation steps, both of which are downhill in the energy profile by -0.69 eV and -0.33 eV , respectively. Finally, $^*\text{PhN}$ is converted to Ph-NNOPh with high priority by a highly exothermic process (-2.15 eV) over $^*\text{PhNH}$ (-1.70 eV). In the case of Co(III) , the conversion of $^*\text{PhNO}_2$ to $^*\text{PhNO}_2\text{H}$ is uphill in the energy profile by 0.58 eV due to the strong adsorption of PhNO_2 . Following the formation of $^*\text{PhNO}_2\text{H}$, its further hydrogenation to $^*\text{PhNO}$ is energetically favorable (-1.86 eV), and then $^*\text{PhNO}$ undergoes two successive hydrogenation steps to generate $^*\text{PhN}$ and which is overall exothermic by -1.08 eV . By overcoming an energy barrier of merely 0.07 eV , $^*\text{PhN}$ can be easily transformed to $^*\text{PhNH}$ compared with a higher energy barrier of 1.17 eV to obtain Ph-NNOPh .

We also performed a kinetic analysis to gain more insights into the reactivity of $\text{Co}_1/\text{Nb}_2\text{O}_5$ and Co(III) . It was found that the kinetic barrier (E_b) of the dissociation of an H_2 molecule on Nb_2O_5 is 0.91 eV (Supplementary Fig. 55), consistent with the previous report (0.88 eV)⁶³. The E_b of $\text{Co}_1/\text{Nb}_2\text{O}_5$ (0.84 eV) is close to that of Nb_2O_5 (Supplementary Fig. 56); this may be due to the fact that H_2 is physically adsorbed on Nb_2O_5 and $\text{Co}_1/\text{Nb}_2\text{O}_5$, of which the adsorption energy E_{H_2} is -0.17 and -0.24 eV , respectively. Specially, in both Nb_2O_5 and $\text{Co}_1/\text{Nb}_2\text{O}_5$, H_2 is preferentially located above the Nb site (Supplementary Fig. 57). The H_2 above the Co_1 site is also physisorbed while being more weakly bound (-0.12 eV). Therefore, H_2 dissociation and PhNO_2 hydrogenation may occur on the Nb_2O_5 and the Co_1 site, respectively. Moreover, as expected, Co(III) exhibits stronger H_2 adsorption than $\text{Co}_1/\text{Nb}_2\text{O}_5$ and Nb_2O_5 (Supplementary Fig. 57), and its E_b is as low as 0.02 eV (Supplementary Fig. 58), which is in agreement with previous studies (0.03 eV)⁶⁴. In the presence of $^*\text{PhNO}_2$, H_2 dissociation on Co(III) is still kinetically favorable (Supplementary Fig. 59). These modeling results are consistent with our H_2 -TPD measurements and H_2 - D_2 exchange experiments. Note that the small E_b of H_2 dissociation on Co(III) should not affect the PhNO_2 adsorption and the subsequent hydrogenation steps, given the stronger adsorption of PhNO_2 compared to H_2 . As H_2 is physisorbed, we also calculated H_2 dissociation on $^*\text{PhNO}_2$ of $\text{Co}_1/\text{Nb}_2\text{O}_5$ via the Eley-Rideal (ER) mechanism and found a small E_b of 0.34 eV (Supplementary Fig. 60).

We then moved our attention to the subsequent hydrogenation steps. For the first four hydrogenation steps, the largest E_b of $\text{Co}_1/\text{Nb}_2\text{O}_5$ occurs in the conversion of $^*\text{PhNOH}$ to $^*\text{PhN}$ (0.84 eV), and that of Co(III) is the conversion of $^*\text{PhNO}$ to $^*\text{PhNOH}$ (0.95 eV). Specifically, $\text{Co}_1/\text{Nb}_2\text{O}_5$ exhibits a favorable E_b of 0.22 eV for facilitating the further coupling of $^*\text{PhN}$ and $^*\text{PhNO}$ to $^*\text{Ph-NNOPh}$, which is lower than that of the competing $^*\text{Ph-NH}$ formation (0.65 eV). By contrast, the hydrogenation of $^*\text{PhN}$ to $^*\text{PhNH}$ on Co(III) requires overcoming a moderate E_b of 1.02 eV , whereas the barrier for the $^*\text{Ph-NNOPh}$ generation is 1.21 eV . It should be noted that the active sites of the niobium oxide component are essential for the dehydration reaction because the Nb site of $\text{Co}_1/\text{Nb}_2\text{O}_5$ exhibits favorable binding to $^*\text{PhNO}$, which promotes the coupling of $^*\text{PhNO}$ and $^*\text{PhN}$. In addition, we explored the influence of solvent on the reaction processes and found that the solvent effect did not change the product selectivity of $\text{Co}_1/\text{Nb}_2\text{O}_5$ and Co(III) (Supplementary Figs. 61 and 62). For example, after considering the solvent effect, the E_b of Ph-NNOPh formation on $\text{Co}_1/\text{Nb}_2\text{O}_5$ (0.49 eV) is still lower than that of the competing $^*\text{Ph-NH}$ formation (0.66 eV). These results are consistent with the experimental observations. The

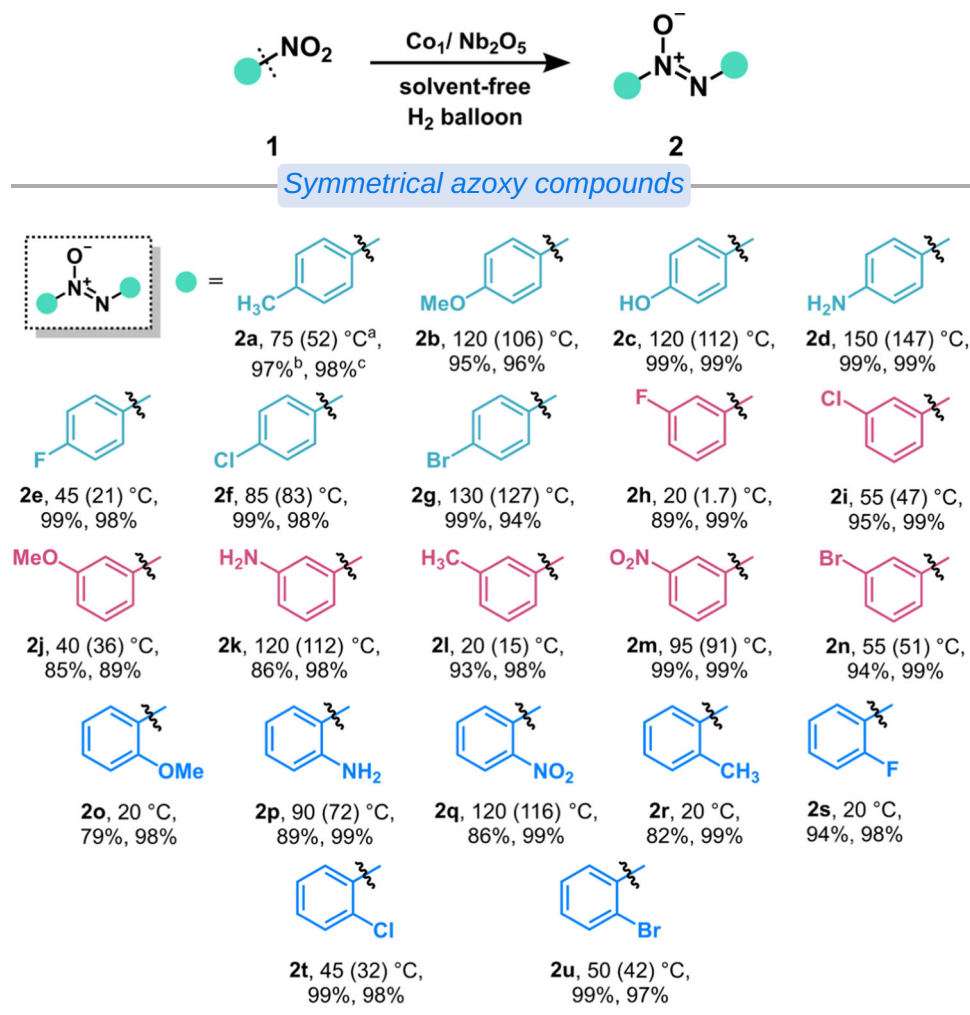


Fig. 5 | Substrate scope of the solvent-free selective hydrogenation of nitroaromatics to symmetrical azoxy compounds. ^a Reaction temperatures and melting points of substrates in parentheses; ^b Conversion; ^c Selectivity.

electronic coupling between Co atoms and adjacent coordinating oxygen atoms in Nb₂O₅ prevents the full hydrogenation of nitroarene, giving rise to a high selectivity towards azoxybenzene. Overall, DFT calculations provide solid evidence that Co₁/Nb₂O₅, with its unique interface and electronic properties and strong electronic metal-support interactions, can significantly affect adsorption characteristics and activation ability with reactants, thus lowering the energy barriers and facilitating the formation of azoxy compounds, which ensures prominent catalytic activity and selectivity.

Discussion

In conclusion, we report on a facile strategy to access an efficient heterogeneous catalyst with atomically dispersed Co atoms over Nb₂O₅ nanomeshes. AC HAADF-STEM, CO-DRIFTS, XAFS, and XPS characterizations reveal that these isolated Co atoms are positively charged and coordinated with the neighboring oxygen atoms. This Co₁/Nb₂O₅ catalyst exhibits exceptional catalytic efficiency in solvent-free hydrogenation of nitrobenzene to give azoxybenzene, superior to that of reported catalysts. In addition, Co₁/Nb₂O₅ successfully promoted the solvent-free hydrogenation coupling of a broad range of nitroaromatics into the desired azoxy compounds with high efficiency. More importantly, excellent recyclability and reaction scale tolerance were demonstrated. Theoretical calculations elucidate that the unique electronic properties and strong electronic metal-support interactions of catalytically active Co sites

in Co₁/Nb₂O₅ have a substantial influence on the reaction pathways and energy barriers. Our findings underscore the great potential of this synthetic strategy for designing high-performance catalysts and provide insights into the structure-performance relationship for industrially important catalytic reactions.

Methods

Synthesis of Nb₂O₅

In a typical synthesis, 1.6 mmol of ammonium niobate oxalate hydrate, 16 mmol of melamine, and 40 mmol of ammonium chloride were dissolved in 40 ml of ethanol and stirred for 12 h. The mixture was then washed with ethanol and vacuum-dried at 80 °C. Subsequently, the dried powder was transferred to a tube furnace and heated at 550 °C in air for 4 h with a heating rate of 2.5 °C min⁻¹. After cooling to room temperature, the white-colored Nb₂O₅ nanomeshes were obtained.

Synthesis of Co₁/Nb₂O₅

In a typical synthesis, 0.4 g of as-prepared Nb₂O₅ was subjected to an incipient wetness impregnation method with 600 μl cobalt(II) acetate ethanol solution (20 mg/ml), followed by an infrared lamp drying step (Co²⁺@Nb₂O₅). The dried powder was sealed in an argon-filled glass vial and microwave-treated at 800 W for 10 s (Microwave Oven, Galanz) to obtain Co₁/Nb₂O₅. The metal loading in the catalyst was determined to be 0.42 wt%.

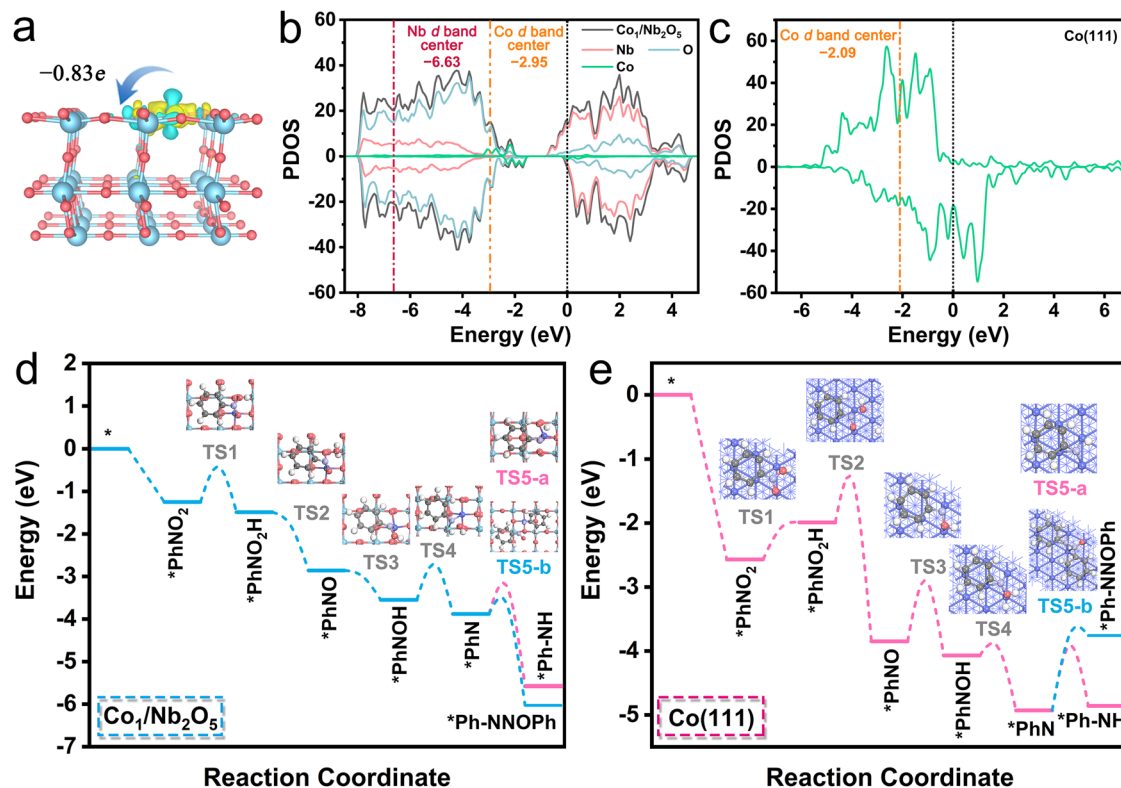


Fig. 6 | DFT calculations. **a** Bader charge and charge density difference of Co₁/Nb₂O₅. The isosurface level is 0.004 eÅ⁻³. The PDOS and *d* band centers of **(b)** Co₁/Nb₂O₅ and **(c)** Co(111). Energy profiles of solvent-free selective hydrogenation of

nitrobenzene over **(d)** Co₁/Nb₂O₅ and **(e)** Co(111). Inset: the corresponding transition state configurations.

Synthesis of Co NPs/Nb₂O₅

The preparation method was the same as that of Co₁/Nb₂O₅, except 1.3 ml of cobalt(II) acetate ethanol solution (100 mg/ml) was used. The metal loading in the catalyst was determined to be 5.12 wt%.

Catalytic evaluation

The solvent-free selective hydrogenation of nitroaromatics on Co₁/Nb₂O₅ was evaluated under atmosphere pressure. Typically, 20 mmol of nitrobenzene and 100 mg of Co₁/Nb₂O₅ (with a molar ratio of 2800:1) were introduced into 25 ml of a round bottom flask connected with a balloon filled with H₂. The catalytic reaction was performed at 20 °C. After the reaction, 50 μl of the resultant mixture was added to 2 ml of ethyl acetate before centrifugation. The corresponding organic compounds were extracted and analyzed by gas chromatography (GC, Techcomp GC-7980) equipped with an HP-5 capillary column and a flame ionization detector. The qualitative analysis was performed by gas chromatography-mass spectrometry (GC-MS, 7890 and 5975 C, Agilent). The used catalyst was separated from the reaction mixture by centrifugation and washed with ethanol before being vacuum-dried at 60 °C for the next catalytic cycle.

For the reaction with solvents, 10 mg of Co₁/Nb₂O₅, 2 mmol of nitrobenzene, and 5 ml of mixed solvents (tetrahydrofuran: H₂O = 4:1, v:v) were added into a 25 ml of Schlenk glass vessel tube with a molar ratio of nitrobenzene: Co is 2800:1. The catalytic reaction was performed at 20 °C under H₂ atmosphere.

The turnover frequency (TOF) values of the catalysts were determined below 10% conversion of the substrate and based on exposed Co atoms. The conversion, selectivity, yield, and TOF are defined as follows:

$$\text{Conversion} = \frac{\text{mole of reacted nitrobenzene}}{\text{mole of nitrobenzene fed}} \times 100\% \quad (1)$$

$$\text{Selectivity} = \frac{\text{mole of azoxybenzene formed}}{\text{mole of nitrobenzene reacted}} \times 100\% \quad (2)$$

$$\text{TOF} = \frac{\text{mole of converted nitrobenzene}}{\text{mole of exposed cobalt atoms} \times \text{reaction time}} \times 100\% \quad (3)$$

$$\text{Yield} = \frac{\text{mole of azoxy compounds} \times 2}{\text{mole of nitrobenzene}} \times 100\% \quad (4)$$

Data availability

The data supporting the findings of this work are available within the article and Supplementary Information. All data are available from the corresponding authors upon request.

References

- Doherty, S. et al. Highly selective and solvent-dependent reduction of nitrobenzene to N-phenylhydroxylamine, azoxybenzene, and aniline catalyzed by phosphino-modified polymer immobilized ionic liquid-stabilized AuNPs. *ACS Catal.* **9**, 4777–4791 (2019).
- Formenti, D., Ferretti, F., Scharnagl, F. K. & Beller, M. Reduction of nitro compounds using 3d-non-noble metal catalysts. *Chem. Rev.* **119**, 2611–2680 (2019).
- Dai, Y. et al. Light-tuned selective photosynthesis of azo- and azoxyaromatics using graphitic C₃N₄. *Nat. Commun.* **9**, 60 (2018).
- Yan, H. et al. Atomic engineering of high-density isolated Co atoms on graphene with proximal-atom controlled reaction selectivity. *Nat. Commun.* **9**, 3197 (2018).
- Zhao, J.-X. et al. Selectivity regulation in Au-catalyzed nitroaromatic hydrogenation by anchoring single-site metal oxide promoters. *ACS Catal.* **10**, 2837–2844 (2020).

6. Lou, Y. et al. Pocketlike active site of Rh₁/MoS₂ single-atom catalyst for selective crotonaldehyde hydrogenation. *J. Am. Chem. Soc.* **141**, 19289–19295 (2019).
7. Ma, Y. et al. High-density and thermally stable palladium single-atom catalysts for chemoselective hydrogenations. *Angew. Chem. Int. Ed.* **59**, 21613–21619 (2020).
8. Jin, H. et al. Sabatier phenomenon in hydrogenation reactions induced by single-atom density. *J. Am. Chem. Soc.* **145**, 12023–12032 (2023).
9. Wu, B. et al. Ru single atoms for efficient chemoselective hydrogenation of nitrobenzene to azoxybenzene. *Green Chem.* **23**, 4753–4761 (2021).
10. Chen, Z., Liu, J., Koh, M. J. & Loh, K. P. Single-atom catalysis: from simple reactions to the synthesis of complex molecules. *Adv. Mater.* **34**, 2103882 (2022).
11. Guo, J. et al. Metal-organic frameworks as catalytic selectivity regulators for organic transformations. *Chem. Soc. Rev.* **50**, 5366–5396 (2021).
12. Kaden, W. E., Wu, T., Kunkel, W. A. & Anderson, S. L. Electronic structure controls reactivity of size-selected Pd clusters adsorbed on TiO₂ surfaces. *Science* **326**, 826–829 (2009).
13. Zaera, F. Designing sites in heterogeneous catalysis: are we reaching selectivities competitive with those of homogeneous catalysts? *Chem. Rev.* **122**, 8594–8757 (2022).
14. Giannakakis, G., Mitchell, S. & Pérez-Ramírez, J. Single-atom heterogeneous catalysts for sustainable organic synthesis. *Trends Chem.* **4**, 264–276 (2022).
15. Clarke, C. J., Tu, W.-C., Levers, O., Bröhl, A. & Hallett, J. P. Green and sustainable solvents in chemical processes. *Chem. Rev.* **118**, 747–800 (2018).
16. Ni, S. et al. Mechanochemical solvent-free catalytic C–H methylation. *Angew. Chem. Int. Ed.* **60**, 6660–6666 (2021).
17. Mi, R. et al. Solvent-free heterogeneous catalytic hydrogenation of polyesters to diols. *Angew. Chem. Int. Ed.* **62**, e202304219 (2023).
18. Miao, Y. et al. Photothermal recycling of waste polyolefin plastics into liquid fuels with high selectivity under solvent-free conditions. *Nat. Commun.* **14**, 4242 (2023).
19. Shi, X. et al. High performance and active sites of a ceria-supported palladium catalyst for solvent-free chemoselective hydrogenation of nitroarenes. *Chem. Cat. Chem.* **9**, 3743–3751 (2017).
20. Sun, Z. et al. The solvent-free selective hydrogenation of nitrobenzene to aniline: an unexpected catalytic activity of ultrafine Pt nanoparticles deposited on carbon nanotubes. *Green Chem.* **12**, 1007–1011 (2010).
21. Di Liberto, G., Tosoni, S., Cipriano, L. A. & Pacchioni, G. A few questions about single-atom catalysts: When modeling helps. *Acc. Mater. Res.* **3**, 986–995 (2022).
22. Liang, X., Fu, N., Yao, S., Li, Z. & Li, Y. The progress and outlook of metal single-atom-site catalysis. *J. Am. Chem. Soc.* **144**, 18155–18174 (2022).
23. Li, H., Li, R., Liu, G., Zhai, M. & Yu, J. Noble-metal-free single- and dual-atom catalysts for artificial photosynthesis. *Adv. Mater.* **13**, 2301307 (2023).
24. Liu, L. & Corma, A. Isolated metal atoms and clusters for alkane activation: translating knowledge from enzymatic and homogeneous to heterogeneous systems. *Chem* **7**, 2347–2384 (2021).
25. Li, Z., Wang, D., Wu, Y. & Li, Y. Recent advances in the precise control of isolated single-site catalysts by chemical methods. *Natl. Sci. Rev.* **5**, 673–689 (2018).
26. Swain, S., Altaee, A., Saxena, M. & Samal, A. K. A comprehensive study on heterogeneous single atom catalysis: current progress, and challenges. *Coord. Chem. Rev.* **470**, 214710 (2022).
27. Ji, S. et al. Construction of a single-atom palladium catalyst by electronic metal-support interaction and interface confinement effect with remarkable performance in Suzuki coupling reaction. *Chem. Eng. J.* **452**, 139205 (2023).
28. Li, Z. et al. Engineering the electronic structure of single-atom iron sites with boosted oxygen bifunctional activity for zinc-air batteries. *Adv. Mater.* **35**, 2209644 (2023).
29. Chen, C. et al. Zero-valent palladium single-atoms catalysts confined in black phosphorus for efficient semi-hydrogenation. *Adv. Mater.* **33**, 2008471 (2021).
30. Yang, H. et al. Catalytically active atomically thin cuprate with periodic Cu single sites. *Natl. Sci. Rev.* **10**, <https://doi.org/10.1093/nsr/nwac100> (2023).
31. Li, Z. et al. A heterogeneous single atom cobalt catalyst for highly efficient acceptorless dehydrogenative coupling reactions. *Small* **19**, 2207941 (2023).
32. Dong, X. et al. Molten salt-induction of geometrically deformed ruthenium single atom catalysts with high performance for aerobic oxidation of alcohols. *Chem. Eng. J.* **451**, 138660 (2023).
33. Guo, Y., Jing, Y., Xia, Q. & Wang, Y. NbO_x-based catalysts for the activation of C–O and C–C bonds in the valorization of waste carbon resources. *Acc. Chem. Res.* **55**, 1301–1312 (2022).
34. Jing, Y., Xin, Y., Guo, Y., Liu, X. & Wang, Y. Highly efficient Nb₂O₅ catalyst for aldol condensation of biomass-derived carbonyl molecules to fuel precursors. *Chin. J. Catal.* **40**, 1168–1177 (2019).
35. Jing, Y. et al. Towards the circular economy: converting aromatic plastic waste back to arenes over a Ru/Nb₂O₅ catalyst. *Angew. Chem. Int. Ed.* **60**, 5527–5535 (2021).
36. Shao, Y. et al. Selective production of arenes via direct lignin upgrading over a niobium-based catalyst. *Nat. Commun.* **8**, 16104 (2017).
37. Xia, J. et al. Identifying the activity origin of a single-atom Au₁/Nb₂O₅ catalyst for hydrodeoxygenation of methylcatechol: A stable substitutional Au⁺ site. *ACS Catal.* **13**, 6093–6103 (2023).
38. Lim, E. et al. Facile synthesis of Nb₂O₅@carbon core-shell nanocrystals with controlled crystalline structure for high-power anodes in hybrid supercapacitors. *ACS Nano* **9**, 7497–7505 (2015).
39. Zheng, Y. et al. Defect-concentration-mediated T-Nb₂O₅ anodes for durable and fast-charging Li-ion batteries. *Adv. Funct. Mater.* **32**, 2107060 (2022).
40. Chen, D. et al. Unraveling the nature of anomalously fast energy storage in T-Nb₂O₅. *J. Am. Chem. Soc.* **139**, 7071–7081 (2017).
41. Zheng, Y. et al. Triple conductive wiring by electron doping, chelation coating and electrochemical conversion in fluffy Nb₂O₅ anodes for fast-charging Li-ion batteries. *Adv. Sci.* **9**, 2202201 (2022).
42. Zhang, Y., Song, T., Zhou, X. & Yang, Y. Oxygen-vacancy-boosted visible light driven photocatalytic oxidative dehydrogenation of saturated N-heterocycles over Nb₂O₅ nanorods. *Appl. Catal. B Environ.* **316**, 121622 (2022).
43. Liu, R. et al. Design of aligned porous carbon films with single-atom Co–N–C sites for high-current-density hydrogen generation. *Adv. Mater.* **33**, 2103533 (2021).
44. Liu, Y. et al. Improving CO₂ photoconversion with ionic liquid and Co single atoms. *Nat. Commun.* **14**, 1457 (2023).
45. Li, L., Dong, L., Liu, X., Guo, Y. & Wang, Y. Selective production of ethylbenzene from lignin oil over FeO_x modified Ru/Nb₂O₅ catalyst. *Appl. Catal. B Environ.* **260**, 118143 (2020).
46. Su, K. et al. Tuning the Pt species on Nb₂O₅ by support-induced modification in the photocatalytic transfer hydrogenation of phenylacetylene. *Appl. Catal. B Environ.* **298**, 120554 (2021).
47. Li, Y. et al. A single site ruthenium catalyst for robust soot oxidation without platinum or palladium. *Nat. Commun.* **14**, 7149 (2023).
48. Shi, X. et al. Protruding Pt single-sites on hexagonal ZnIn₂S₄ to accelerate photocatalytic hydrogen evolution. *Nat. Commun.* **13**, 1287 (2022).

49. Singh, J. A. et al. Understanding the active sites of CO hydrogenation on Pt–Co catalysts prepared using atomic layer deposition. *J. Phys. Chem. C* **122**, 2184–2194 (2018).
50. Kumar, N., Jothimurugesan, K., Stanley, G. G., Schwartz, V. & Spivey, J. J. In situ FT-IR study on the effect of cobalt precursors on CO adsorption behavior. *J. Phys. Chem. C* **115**, 990–998 (2011).
51. Song, D., Li, J. & Cai, Q. In situ diffuse reflectance FTIR study of CO adsorbed on a cobalt catalyst supported by silica with different pore sizes. *J. Phys. Chem. C* **111**, 18970–18979 (2007).
52. Kumar, P. et al. High-density cobalt single-atom catalysts for enhanced oxygen evolution reaction. *J. Am. Chem. Soc.* **145**, 8052–8063 (2023).
53. Wang, N. et al. Doping shortens the metal/metal distance and promotes OH coverage in non-noble acidic oxygen evolution reaction catalysts. *J. Am. Chem. Soc.* **145**, 7829–7836 (2023).
54. Shi, Z. et al. Enhanced acidic water oxidation by dynamic migration of oxygen species at the Ir/Nb₂O_{5-x} catalyst/support interfaces. *Angew. Chem. Int. Ed.* **61**, e202212341 (2022).
55. Chen, X. et al. Structure-dependence and metal-dependence on atomically dispersed Ir catalysts for efficient n-butane dehydrogenation. *Nat. Commun.* **14**, 2588 (2023).
56. Feng, Z. et al. Asymmetric sites on the ZnZrO_x catalyst for promoting formate formation and transformation in CO₂ hydrogenation. *J. Am. Chem. Soc.* **145**, 12663–12672 (2023).
57. Lee, J. D. et al. Facilitating hydrogen dissociation over dilute nanoporous Ti–Cu catalysts. *J. Am. Chem. Soc.* **144**, 16778–16791 (2022).
58. Zhao, H. et al. The role of Cu₁-O₃ species in single-atom Cu/ZrO₂ catalyst for CO₂ hydrogenation. *Nat. Catal.* **5**, 818–831 (2022).
59. Kyriakou, G. et al. Isolated metal atom geometries as a strategy for selective heterogeneous hydrogenations. *Science* **335**, 1209–1212 (2012).
60. Liu, W. et al. Highly-efficient RuNi single-atom alloy catalysts toward chemoselective hydrogenation of nitroarenes. *Nat. Commun.* **13**, 3188 (2022).
61. Richner, G., van Bokhoven, J. A., Neuhold, Y.-M., Makosch, M. & Hungerbühler, K. In situ infrared monitoring of the solid/liquid catalyst interface during the three-phase hydrogenation of nitrobenzene over nanosized Au on TiO₂. *Phys. Chem. Chem. Phys.* **13**, 12463–12471 (2011).
62. Liu, L., Concepción, P. & Corma, A. Modulating the catalytic behavior of non-noble metal nanoparticles by inter-particle interaction for chemoselective hydrogenation of nitroarenes into corresponding azoxy or azo compounds. *J. Catal.* **369**, 312–323 (2019).
63. Zhou, H. et al. Hydrogenolysis cleavage of the C_{sp}²–C_{sp}³ bond over a metal-free NbOPO₄ catalyst. *ACS Catal.* **12**, 4806–4812 (2022).
64. Yu, M. et al. High coverage H₂ adsorption and dissociation on fcc Co surfaces from DFT and thermodynamics. *Int. J. Hydrog. Energy* **43**, 5576–5590 (2018).

Acknowledgements

This work was supported by the Outstanding Youth Project of the Natural Science Foundation of Heilongjiang Province (YQ2022B002), the Scientific Research Foundation for Returned Scholars of Heilongjiang Province of China (719900091), and the Heilongjiang Touyan Innovation Team Program. Y.W. acknowledges financial supports from the Natural Science Foundation of China (22203044) and the Jiangsu Specially

Appointed Professor Plan. The authors thank beamline 1W1B of Beijing Synchrotron Radiation Facility (BSRF) in Beijing and beamline of MCD-A and MCD-B (Soochow Beamline for Energy Materials) of National Synchrotron Radiation Laboratory in Hefei for XAS measurements. The authors also acknowledge the Catalysis and Surface Science Endstation at beamline BL11U for support in ultraviolet photoemission spectroscopy (UPS) measurements.

Author contributions

Z.L. conceived the idea, supervised the project, and wrote the paper. Xi.L. synthesized the catalysts, performed the catalytic reactions, and analyzed the data. Co.G. and Y.W. conducted the DFT calculations. S.J., H.L., Ch.G., Xu.L., and S.X. assisted with the material synthesis and characterizations. S.J. and H.L. performed the in-situ FT-IR measurements and analyzed the data. B.L. and W.W. performed H₂-TPR, H₂-TPD, H₂-D₂ exchange, and TGA measurements. C.W. and W.Y. helped with the analysis of the XAFS spectra. J.H.H. contributed to the discussion on the experiment. All authors contributed to the overall scientific interpretation and edited the manuscript.

Competing interests

The authors declare no competing interests.

Additional information

Supplementary information The online version contains supplementary material available at <https://doi.org/10.1038/s41467-024-47402-5>.

Correspondence and requests for materials should be addressed to Zhijun Li or Yu Wang.

Peer review information *Nature Communications* thanks Huizhen Liu, Jiong Lu and the other, anonymous, reviewer for their contribution to the peer review of this work. A peer review file is available.

Reprints and permissions information is available at <http://www.nature.com/reprints>

Publisher's note Springer Nature remains neutral with regard to jurisdictional claims in published maps and institutional affiliations.

Open Access This article is licensed under a Creative Commons Attribution 4.0 International License, which permits use, sharing, adaptation, distribution and reproduction in any medium or format, as long as you give appropriate credit to the original author(s) and the source, provide a link to the Creative Commons licence, and indicate if changes were made. The images or other third party material in this article are included in the article's Creative Commons licence, unless indicated otherwise in a credit line to the material. If material is not included in the article's Creative Commons licence and your intended use is not permitted by statutory regulation or exceeds the permitted use, you will need to obtain permission directly from the copyright holder. To view a copy of this licence, visit <http://creativecommons.org/licenses/by/4.0/>.

© The Author(s) 2024